Modelling of graphene Q-switched Tm lasers

A.S. Yasukevich[1], P. Loiko[2], N.V. Gusakova[1], J.M. Serres[3], X. Mateos[3,4,*], K.V. Yumashev[1], N.V. Kuleshov[1], V. Petrov[4], U. Griebner[4], M. Aguiló[3] and F. Díaz[3]

[1]Center for Optical Materials and Technologies, Belarusian National Technical University, 65/17 Nezavisimosti Ave., Minsk, Belarus 220013
[2]ITMO University, Kronverkskiy pr., 49, Saint-Petersburg, 197101, Russia
[3]Física i Cristal·lografia de Materials i Nanomaterials (FiCMA-FiCNA), Universitat Rovira i Virgili (URV), Campus Sescelades, c/ Marcel·lí Domingo, s/n., Tarragona, Spain E-43007
[4]Max Born Institute for Nonlinear Optics and Short Pulse Spectroscopy, 2A Max-Born-Str., Berlin, Germany D-12489

*Corresponding author, e-mail: xavier.mateos@urv.cat, mateos@mbi-berlin.de

Abstract We report on a model of diode-pumped Thulium lasers passively Q-switched by a graphene saturable absorber applicable also for any other "fast" saturable absorber. It reasonably predicts the dependence of the pulse duration, pulse energy and pulse repetition frequency on the absorbed power. The model is applied in the present work for a Tm:KLuW microchip laser passively Q-switched with a multi-layer graphene saturable absorber. The laser generates ~1 W at 1926 nm with a slope efficiency of 39%. Stable 190 ns / 4.1 μJ pulses are achieved at a pulse repetition frequency of 260 kHz. The potential of graphene for the generation of few-ns pulses at ~2 μm is discussed.

Keywords: thulium laser, diode-pumped laser, Q-switching, graphene

1. Introduction

Thulium (Tm^{3+}) is a laser-active ion that provides an emission at ~2 µm due to the $^3F_4 \rightarrow {}^3H_6$ electronic transition [1]. This emission finds applications in medicine (due to the strong absorption of water at this wavelength) and remote sensing of water and CO_2 in the atmosphere. A common approach to produce laser pulses from a solid-state laser is the passive Q-switching (PQS) technique, which is realized by the insertion of an appropriate saturable absorber (SA) into the laser cavity. Conventional "bulk" SAs for Tm lasers are based on zinc chalcogenides, Cr:ZnS and Cr:ZnSe, which enable the generation of Q-switched pulses with high energies at low pulse repetition frequencies (PRFs) [2,3]. Recently, novel SAs for Tm lasers based on carbon nanostructures have attracted a lot of attention, including graphene [4], graphene oxide [5] and single-walled carbon nanotubes [6].

Focusing on graphene, this material is composed of a single layer of carbon atoms arranged in a honeycomb lattice [7]. It shows broadband and almost wavelength-insensitive linear absorption [8] from ~0.6 µm up to at least ~3 µm and also broadband saturable absorption [9]. Consequently, graphene can be used as "universal" SA for near-IR lasers, including those based on Tm. It shows relatively low saturation intensity, reasonable non-saturable losses, high laser damage threshold and ultrafast recovery time [10-12]. In addition, the control of the modulation depth is possible by varying the number of graphene layers [9]. Graphene saturable absorbers (GSAs) may enable the generation pulses at high PRFs, typically ranging from hundreds of kHz to few MHz. Recently, PQS of bulk Tm lasers with graphene has been realized [4,13,14]. The potential of graphene for the generation of ns pulses in Tm lasers at ~2 µm has also been shown [15].

In the present work, we aimed at a theoretical description of PQS of Tm lasers by a GSA. It enables the prediction of the pulse characteristics as well as their dependence on the absorbed pump power. To verify the validity of our model, a laser based on a Tm:$KLu(WO_4)_2$ crystal (Tm:KLuW) is experimentally investigated. It belongs to the family of monoclinic double tungstates (DTs), which are very suitable hosts for Tm doping [16]. Tm-doped DTs offer intense and broad absorption and emission bands for different polarizations [17,18], and high doping concentrations are possible [19] without significant changes in the crystalline structure and spectroscopic properties. Efficient Tm-doped DT lasers operating in the continuous-wave (CW) [20-22] and the PQS [23-25] regime have been reported previously. As laser set-up, we selected the microchip geometry [26] where both the laser crystal and SA are placed in a compact plano-plano cavity. In particular for GSA, such a set-up is useful for the generation of shorter pulses in the ns range due to the significant reduction of the cavity roundtrip time [15,27].

2. Theoretical model

2.1 Tm laser system

First, let us discuss the energy level scheme of the Tm^{3+} ion, see Fig. 1. Excitation of Tm lasers is usually at ~0.8 µm ($^3H_6 \rightarrow {}^3H_4$ transition), which matches very well the emission of AlGaAs laser diodes. Laser operation is achieved typically at ~1.95 µm due to the $^3F_4 \rightarrow {}^3H_6$ transition. This results in a low Stokes efficiency, $\eta_{St} = \lambda_p/\lambda_L \sim 0.41$. However, a special feature of the Tm^{3+} system is the very strong cross-relaxation (CR) mechanism for two adjacent ions, $^3H_4 + {}^3H_6 \rightarrow {}^3F_4 + {}^3F_4$ [1,28]. This process ideally generates two photons at ~1.95 µm from only one

pump photon at ~0.8 μm, resulting in a much higher η_{St} of $2\lambda_p/\lambda_L$ ~0.82. Laser operation with strong CR is very desirable for the increase of the laser slope efficiency and the reduction of heat loading. The latter can be estimated as $\eta_h = 1 - 2\lambda_p/\lambda_L$ ~0.18 which is lower than for Nd^{3+} ions (η_h ~0.24) pumped at the same wavelength. For the main hosts implemented for Tm^{3+} doping, e.g. YAG, YLF or KLuW [1,18,29], a very high CR efficiency for reasonable Tm^{3+} doping concentrations (3-5 at.%) was demonstrated and, consequently, high laser efficiency was achieved [30].

The excited-state absorption (ESA) is an important effect limiting the performance of lanthanide-based lasers. ESA leads to a depopulation of the pump level or emitting state with the excitation of the lanthanide ions to higher-lying multiplets thus being part of up-conversion luminescence (UCL) processes. Non-radiative or radiative UCL transitions from these multiplets result in an additional heat loading and decrease the laser efficiency. When pumping Tm^{3+} ions at ~0.8 μm, $^3H_5 \rightarrow {}^1G_4$ ESA may occur. It results in the population of the $^1G_4$ higher-lying multiplet (~21500 cm^{-1}) from which several visible up-conversion emissions occur at ~480 nm (to the $^3H_6$ ground-state, observed in the blue), at ~650 nm (to the $^3F_4$ state, in the red) and at ~800 nm (to the $^3H_5$ state, in the near-IR). However, for high Tm^{3+} concentrations, a second efficient CR process is possible, $^1G_4 + {}^3H_6 \rightarrow {}^3F_{2,3} + {}^3F_4$ [18]. As the energy gap between the $^3F_{2,3}$ states and the lower-lying $^3H_4$ pump level is small (~2000 cm^{-1}), a fast non-radiative relaxation suppresses any additional parasitic emissions. Consequently, UCL in single Tm^{3+}-doped materials is weak.

Considering a fast and efficient CR mechanism for highly Tm^{3+}-doped laser materials, one can neglect the population of all multiplets with the exception of the $^3H_6$ ground state (N_1) and the $^3F_4$ upper laser level (N_2), so $N_1 + N_2 \approx N_{Tm}$ where N_{Tm} is the Tm^{3+} concentration. In particular, for Tm:KLuW crystals with a doping level >3 at.%, the quantum efficiency for ~0.8 μm excitation is η_q > 1.98, almost approaching the theoretical value of 2 and the quantum yield of the luminescence from the $^3F_4$ state is >0.99 [30]. As a consequence, <1% of the Tm^{3+} ions can potentially be excited into higher-lying multiplets. In the present paper for the sake of simplicity we will describe the PQS Tm laser by considering the rate equations only for the two multiplets (|1> = $^3H_6$ and |2> = $^3F_4$) involved in the laser emission. PQS is realized by GSA.

2.2 Rate equations

Graphene, when applied for PQS of a Tm laser, should be considered as a "fast" SA because the recovery of the initial absorption is much faster than the characteristic time of pulse formation in the Tm laser (from tens to hundreds of ns). Graphene has two characteristic recovery times, the "fast" component is about 100 fs and a "slow" one in the order of 1 ps. They are related (i) to thermalization due to ultrafast intraband carrier-carrier and carrier-optical phonon scattering resulting in a Fermi-Dirac distribution in the valence band and (ii) to much slower electron-hole recombination, respectively [12].

To model the characteristics of a GSA PQS of a Tm laser, we solved the system of rate equations for a quasi-three-level laser material with a "fast" SA. These equations are written for two variables: (i) I_L – radiation intensity in the laser crystal at the laser frequency v_L and (ii) N_2 - population of the upper laser level:

$$\frac{dI_L}{dt} = \frac{c\mu}{n}[k_L - k_{loss} - \frac{1}{l_{AM}}\alpha'(I_L)]I_L + I'_{noise}, \quad (1a)$$

$$\frac{dN_2}{dt}=\eta_q\frac{I_p}{h\nu_p}k_p-\frac{I_L}{h\nu_L}k_L-\frac{N_2}{\tau}. \quad (1b)$$

Here, k_L is the gain coefficient and k_{loss} is the resonator loss coefficient at the laser frequency ν_L:

$$k_L=N_2\sigma_{SE}^L-(N_{Tm}-N_2)\sigma_{abs}^L, \quad (2)$$

$$k_{loss}=-\frac{1}{2l_{AM}}[\ln(1-T_{OC})+\ln(1-L)]. \quad (3)$$

In Eq. (1), α' is the absorption of graphene which is a function of I_L (see below). The resonator and material parameters used in the formulas are as follows: $\mu = l_{AM}n_{AM}/l_c$ is the resonator filling factor; l_{AM} is the active medium (AM) length; n_{AM} is the refractive index of the active element; l_c is the optical length of the resonator; ν_p and ν_L are the pump and laser frequencies, respectively; T_{OC} is the transmission of the output coupler and L is the round trip passive intracavity loss; I'_{noise} is the rate of noise intensity; σ^L_{SE} and σ^L_{abs} are the stimulated-emission (SE) and absorption cross-sections of the AM at the laser frequency, respectively; η_q is the quantum efficiency for the AM (the number of emitted ~2 μm photons due to one absorbed ~0.8 μm pump photon), τ is the lifetime of the upper laser level ($^3F_4$ level of Tm^{3+}). The fundamental constants: c is the light velocity and h is the Planck constant. The average pump intensity in the active element, I_p, is expressed as:

$$I_p=\frac{P_{inc}}{\pi w_p^2}\frac{1-\exp(-k_p l_{AM})}{k_p l_{AM}}, \quad (4a)$$

$$k_p=(N_{Tm}-N_2)\sigma_{abs}^p. \quad (4b)$$

Here, P_{inc} is the incident pump power and w_p is the pump spot radius, k_p is the absorption coefficient for the pump radiation and σ^p_{abs} is the absorption cross-section of the AM at the pump frequency ν_p. The pump and laser intensities, populations, loss and gain coefficients are considered as averaged over the crystal volume.

The solution of the system of rate equations is performed for normalized variables, $N_2^* = N_2/N_{Tm}$ and $I_L^* = I_L/I_{sat}$, as well as normalized time $t^* = t/\tau_{ph}$ where τ_{ph} is the lifetime of the photons in the cavity, $\tau_{ph} = n/(c\mu k_{loss})$. This solution yields a time-dependent intracavity laser intensity $I_L(t)$ which is used to calculate the output laser power:

$$P_{out}(t)=I_L(t)k_{act}\frac{\pi w_L^2}{2}l_{AM}, \quad (5a)$$

$$k_{act}=-\frac{1}{2l_{AM}}\ln(1-T_{OC}). \quad (5b)$$

Here, w_L is the radius of the laser Gaussian mode and k_{act} is the coefficient of useful losses on the OC. From the time-dependent $P_{out}(t)$, we calculated the pulse duration $\Delta\tau$ (as FWHM), the pulse energy E_{out} and the PRF for the Q-switched pulses.

2.3 Saturable absorption of graphene

A single-layer graphene is known for its "universal" small-signal absorption, which is almost constant in a wide wavelength range spanning from the visible (~0.6 μm) up to at least ~3 μm. This absorption is relatively large if considering the presence of a single layer of atoms, $\alpha' \approx \pi\alpha = 2.3\%$

where $\alpha = e^2/\hbar c \approx 1/137$ is the fine structure constant [8]. For samples containing several carbon layers (n), the small-signal absorption is scaling with n following an almost linear law, $\alpha' \approx n\pi\alpha$. The total absorption of graphene can be separated in two parts, the saturable, α'_S, and the non-saturable one, α'_{NS}. Thus, the internal small- signal transmission of graphene can be represented as $T = 1 - \alpha' = 1 - (\alpha'_S + \alpha'_{NS})$.

The dependence of the total absorption of graphene on the laser intensity is [10]:

$$\alpha'(I_L) = \alpha'_{NS} + \frac{\alpha'_S}{1+(I_L/I_{sat})}. \quad (6)$$

Here, I_{sat} is the saturation intensity, which corresponds to 2-fold decrease of the saturable part of the graphene absorption. The laser intensity in Eq. (6) is the one in the SA, which is related to the laser intensity in the AM as $I_L(SA) = \chi \times I_L(AM)$, where χ is the ratio of mode areas in the AM and SA, $\chi = w_L^2(AM)/w_L^2(SA)$. For microchip lasers, $\chi \sim 1$. Consequently, I_L used in Eq. (1) and Eq. (6) are the same intensity. Eq. (6) is a particular case of the time-independent form of the fast saturable absorber equation [31].

The mechanism of saturable absorption of graphene is schematically represented in Fig. 2. Graphene has a unique band structure. Both its valence and conduction bands (VB and CB, respectively) have a shape of hollow cones and they are touching each other resulting in almost zero bandgap. The absorption of a photon with an energy $h\nu$ leads to the formation of a hole in the VB and an electron in the CB. For high excitation intensities, the concentration of photogenerated carriers increases significantly, so that the states near the edges of VB and CB (within the energy interval of $h\nu/2$ for each band) are filled. The band-filling occurs because two electrons cannot fill the same state in agreement with the Pauli blocking principle [10,11]. Thus, further absorption is blocked implying transparency of graphene.

Although the linear absorption of graphene is almost wavelength-independent, its nonlinear properties show strong dispersion [9]. In particular, I_{sat} decreases with the decrease of the photon energy $h\nu$ (i.e., it is easier to achieve the saturation of graphene at longer wavelengths). Figure 2 illustrates this dependence because the illumination of graphene with lower energy photons requires the excitation of less number of electrons in order to exhaust the corresponding part of the VB and to observe the absorption saturation. According to experimental studies [9], I_{sat} decreases almost linearly with the decrease of $h\nu$ in the ~0.5...2 μm spectral range and it approaches zero for $h\nu \rightarrow 0$, which is the characteristic of the Dirac point in the graphene band structure. Thus, the use of graphene as SA for ~2 μm lasers (e.g., Tm or Ho-lasers) is more attractive compared with those emitting at ~1 μm. This characteristic feature was confirmed by the greater difficulty to achieve stable GSA PQS of ~1 μm solid-state lasers without additional mode confinement like in waveguide or fiber configurations [32].

For samples with number of carbon layers $n > 1$, as mentioned above, the linear absorption is scaling with n. However, its saturable part, α'_S/α', decreases with n [9,10]. This is related to the increased non-saturable loss due to multiple scattering on the layer-to-layer interfaces and defects in the graphene structure. The increase of n leads also to a slight reduction of I_{sat}. From the experimental results on the absorption saturation of single- and multi-layer graphene one can conclude that the optimum value of n is 3...4 as it provides sufficiently large modulation depth while keeping reasonably low non-saturable losses [9].

2.4 Noise estimation

The rate of noise intensity I'_{noise} is determined by spontaneous emission in the laser mode. The time dependent power density of spontaneous emission u_{sp} is determined as:

$$\frac{\mathrm{d}u_{\mathrm{sp}}}{\mathrm{d}t} = h\nu_{\mathrm{L}}\frac{N_2}{\tau_{\mathrm{rad}}}, \tag{7}$$

where τ_{rad} is radiative lifetime of the upper laser level ($^3F_4$ level of Tm^{3+}). This power is emitted into the total space angle 4π. Considering the emission into the laser mode with a space angle Ω_{L} and taking into account that this emission occurs in two directions, the value of I'_{noise} is:

$$I'_{\mathrm{noise}} = \frac{\mathrm{d}u_{\mathrm{sp}}}{\mathrm{d}t}\frac{2\Omega_L}{4\pi}\frac{c}{n}. \tag{8}$$

The space angle is $\Omega_{\mathrm{L}} = \pi\theta_{\mathrm{L}}^2$ where θ_{L} is the divergence of the Gaussian laser beam in the active crystal. Finally, one obtains:

$$I'_{\mathrm{noise}} = \frac{hc^2 N_2 \lambda_{\mathrm{L}}}{2\pi^2 n^3 w_L^2 \tau_{\mathrm{rad}}}. \tag{9}$$

3. Results and discussion

3.1 Laser set-up

The main reason for the relatively long (typically few μs) durations achieved when PQS Tm bulk lasers with long cavities using graphene [4,13,14] is related to the low modulation depth of GSA (~0.1%) in this case. The main advantage of such cavities is the possibility to avoid unwanted heating of graphene by residual pump absorption. Shortening of the pulse duration can be achieved by using the microchip concept due to the significantly reduced cavity roundtrip time [15]. In the microchip laser, the AM and SA are placed in a plano-plano cavity with minimum separations. Note that, in principle, heating of the SA by residual pump radiation can be avoided also in the microchip laser, by applying suitable coatings to the AE. Here we analyze the PQS results obtained with a Tm:KLuW microchip laser using GSA.

The studied laser crystal, a 3 at.% Tm:KLuW, was grown by the Top-Seeded-Solution Growth (TSSG) slow-cooling method [16]. The Tm:KLuW crystal is monoclinic (sp. group C^6_{2h} - *C2/c*) and opticaly biaxial. The actual concentration of Tm^{3+} ions determined with Electron Probe MicroAnalysis (EPMA) was $N_{\mathrm{Tm}} = 2.15\times10^{20}$ at/cm^3. From the as-grown bulk, a 2.5 mm-thick rectangular sample was cut along the N_{g} axis of the optical indicatrix. This cut provides a positive thermal lens of the active element [33], which is required for mode stabilization in the microchip cavity [22]. Both the $N_{\mathrm{p}}\times N_{\mathrm{m}}$ crystal faces with dimensions 3.0×3.0 mm^2 were polished to laser quality and remained uncoated. The crystal was mounted in a Cu-holder providing cooling from all four lateral sides and Indium foil ensured good thermal contact. The holder was water-cooled down to 12°C.

The plano-plano cavity of the microchip laser, Fig. 3, consisted of a pump mirror (PM) AR-coated for 0.77–1.05 μm and high-reflection (HR) coated for 1.80–2.08 μm, and an output coupler (OC) with transmittance T_{OC} = 5 % at the laser wavelength. Between the second face of the crystal and the OC, a commercial transmission-type GSA (graphene supermarket) was inserted. The GSA

consisted of a 1.05 mm-thick fused silica substrate with multi-layer graphene deposited by chemical vapor deposition (CVD). Its initial small-signal absorption at the laser wavelength was $\alpha' = 5.5\%$, Fig. 4(a). For the single-layer graphene deposited under same conditions, $\alpha' = 2.3\%$, in perfect agreement with the theoretical value. Thus, the mean number of graphene layers in the used sample was $n = 2.4$ (between 2 to 3 layers). The number of carbon layers was confirmed by Raman spectroscopy, Fig. 4(b), according to the relative intensity of the 2D and G peaks. All optical elements were contacted without air gaps, thus the total geometrical cavity length amounted to ~4.05 mm.

As a pump source we used an AlGaAs fiber coupled laser diode (fiber core diameter: 200 μm, N.A.: 0.22) emitting at ~805 nm. The unpolarized pump radiation was collimated and focused into the crystal using a lens assembly (1:1 imaging ratio, 30 mm focal length) resulting in a pump spot radius w_p in the crystal of 100±5 μm. The confocal parameter for the pump beam was $2z_R$ ~3.0 mm. The measured single-pass absorption in the crystal was 47 ±2%. According to the pump spot size, the sensitivity factors of the thermal lens in Tm:KLuW are $M = 12.9$ and 8.1 m^{-1}/W for the directions parallel to the N_p and N_m axes, respectively [33]. The calculated radii of the laser mode in the AM and in the GSA for the "hot" cavity are almost the same, $w_L = 85\pm5$ μm.

A fast InGaAs photodiode (rise time: 200 ps) and a 2 GHz Tektronix DPO5204B digital oscilloscope were used for the detection of the Q-switched pulses.

3.2 Output characteristics

Using the commercial GSA stable PQS was achieved with the Tm:KLuW laser. The corresponding input-output curve is shown in Fig. 5. The maximum average output power was 1064 mW with a slope efficiency $\eta = 39\%$ (with respect to the absorbed power). The laser emission was linearly polarized, $E \parallel N_m$, naturally selected by the anisotropy of the gain [20]. The laser threshold was at $P_{abs} = 2.3$ W and the optical-to-optical efficiency amounted to ~22%. The conversion efficiency with respect to the CW mode of operation was $\eta_{conv} = 70\%$. The output dependence was clearly linear showing no influence of detrimental thermal effects. The typical laser emission spectrum shown in Fig. 5 (inset) consists of one intense peak centered at $\lambda_L = 1926$ nm. This relatively short wavelength is caused by the high intracavity losses due to the non-saturable absorption of the GSA and, hence, a high inversion ratio (β ~0.25, as determined from the rate equations). For this β, λ_L is in agreement with the gain curves of Tm:KLuW [18].

For the GSA Q-switched Tm:KLuW laser, an upper limit for stable PQS existed. Q-switching instabilities are attributed to heating of the GSA by residual (non-absorbed) pump. Due to a large non-saturable loss of the SA (α'_{NS} ~5.3%, see below), ~2.5% of the incident pump power was absorbed by the GSA. Graphene possesses a very high thermal conductivity, κ ~5000 W/mK [34] but it was deposited on a passively-cooled fused silica substrate with much lower thermal conductivity, $\kappa = 1.3$ W/mK. Consequently, heating of the two materials is expected and both of them exhibit thermal expansion. Graphene has a negative coefficient of thermal expansion, $\alpha_t = -7\times10^{-6}$ K^{-1} [35]. In contrast, for the fused silica, α_t is positive, 0.5×10^{-6} K^{-1}. This mismatch causes a compressive strain in the graphene layer with rising temperature and can lead to its slip or buckling from the substrate surface. Thus, increased scattering on the graphene/substrate interface is

expected, which will reduce the saturable absorption of the GSA. Nevertheless, no damage of GSA was observed during laser operation.

The pulse characteristics (duration, energy, PRF and peak power) for the Tm:KLuW laser exhibit a clear dependence on the pump level, Fig. 6. The pulse duration decreased from 510 to 190 ns which was accompanied by an increase of the pulse energy from 0.2 to 4.1 μJ. The laser operated at a PRF ranging from 150 to 260 kHz. The peak power increased almost linearly from 0.4 to 21.6 W.

All these dependences were modeled as described above. The set of material parameters was taken from the literature [9,18], and their values are listed in Table 1. The noise rate I'_{noise} was first estimated in accordance with Eq. (9) and then slightly varied in order to observe the pulsed behavior of the laser output. The modeling results on pulse duration, pulse energy, PRF and peak power are shown in Fig. 6 as solid curves. The error in the calculated pulse characteristics was about ~20%, determined mainly by the precision of the used material parameters. One can see that the modeling is in rather good agreement with the experiment, not only in terms of the absolute values of pulse characteristics but also their dependences on the absorbed power (within the specified error). At the highest studied pump level, the model predicts the generation of 175 ns / 3.8 μJ pulses, which is also close to the experimental results.

For the GSA PQS of the Tm laser, the pulse duration decreases with the absorbed power while the pulse energy increases. This behavior is qualitatively different from Tm laser PQS with a "slow" SA where the pulse duration and energy are weakly dependent on the absorbed power when proper conditions for the saturation of the SA are realized [23-25]. The PRF and peak power in Fig. 6 exhibit almost linear dependence on the absorbed power.

It is worth discussing the modulation depth of the GSA. From the absorption saturation experiment performed in [9], the ratio of the saturable absorption to the total one, α'_S/α', was determined to be 0.65 (single-layer graphene, i.e. $\alpha'_S = 1.5\%$) and 0.58...0.37 (multi-layer graphene, depending on the number of layers). Our former studies of GSAs [36,37] provided an estimation of the modulation depth of $\alpha'_S = 0.10\pm0.02\%$ for the single-layer graphene or $\alpha'_S/\alpha' \sim 0.04$. From this ratio, we estimated α'_S for the multi-layer graphene used in this work as $\alpha'_S = 0.23\pm0.02\%$ (cf. Table 1), which results in good agreement between experiment and modelling. Thus, the actual modulation depth of the GSA is much lower than expected from the absorption saturation measurements.

In order to explain the pump-dependence of pulse characteristics in the GSA passively Q-switched Tm:KLuW laser, we have calculated inracavity peak on-axis intensity of laser radiation at the SA, I_{in}, and the intensity-dependent absorption of the GSA, $\alpha'(I_{in})$. The intracavity intensity is determined as:

$$I_{\text{in}} = \frac{2 - T_{OC}}{T_{OC}} \frac{2E_{out}}{\pi w_L^2 \Delta\tau^*}, , \qquad (10)$$

where it is taken into account that laser mode has a Gaussian spatial profile (TEM_{00} mode) and the temporal profile of the laser pulse is close to Gaussian (so $\Delta\tau^* \approx 1.06\Delta\tau$ is the effective pulse duration). The absorption of GSA is then calculated with Eq. (6). The results are shown in Fig. 7. With the increase of the absorbed pump power, I_{in} increases monotonously from 0.1 to 7.0 MW/cm^2 which results in the bleaching of the GSA. The variation of $\alpha'(I_{in})$ is much stronger close

to the laser threshold due to low intracavity laser intensity and the GSA is almost completely bleached at P_{abs} > 4.5 W that correspond to almost constant $\alpha'(I_{in})$ and, hence, almost unchanged pulse characteristics, as shown in Fig. 6. Thus, we can conclude that the pump-dependence of pulse characteristics in graphene Q-switched lasers is mainly due to variable saturation and, hence, modulation depth of the SA.

From Fig. 7(a), one can estimate the laser-induced damage threshold (LIDT) for the studied GSA to be at least ~7 MW/cm^2 for ns-pulses.

In Fig. 8(a), we present the oscilloscope traces of the single Q-switched pulses observed close to the laser threshold (at P_{abs} = 2.5 W) and at the maximum studied pump level (P_{abs} = 4.9 W). The shortening of the pulse duration with the increase of absorbed power is obvious from this figure. The temporal shape of the pulses is almost symmetric. In Fig. 8(b), the oscilloscope trace of the pulse train corresponding to the maximum PRF = 260 kHz is shown. The intensity fluctuations in the train are ~15%. They are mainly attributed to the above mentioned heating of the GSA.

In Fig. 9(a,b), we present the typical results from the modelling of the GSA PQS Tm:KLuW laser output, $P_{out}(t)$ at a P_{abs} = 4.9 W. The developed model allowed us to predict the onset of lasing and the transition between the CW and PQS operation modes, see Fig. 9(c-f). Here, time is counted from the moment when the pump is switched on (t = 0) and the (c-f) plots differ from the value of the normalized rate of noise intensity, $I'_{norm} = I'_{noise}\tau_{ph}/I_{sat}$, similarly to [37]. I'_{noise} is proportional to the population of the upper laser level N_2. With a misalignment of the laser, the inversion increases to produce higher gain in order to compensate for the increased loss so that I'_{noise} is also increased. This is accompanied by the transition from the generation of intense and short (hundreds of ns) pulses without any CW pedestal ("true" Q-switched behavior) to a modulation of the output signal with long (few μs) pulses showing a CW pedestal and finally to the "true" CW lasing.

3.3 Discussion

The proposed modelling allows one to analyze the influence of various parameters on the performance of GSA PQS of Tm lasers. When considering the SA, the most critical parameter is its saturable absorption. Increasing α'_S results in an increase of the pulse energy and in shortening of the pulse duration, as expected from the general theory of Q-switching. In the case of graphene, α'_S can be varied to a certain extent by changing the number of graphene layers n. Indeed, the results achieved in the present work (190 ns / 4.1 μJ pulses for $n \approx 2.4$) are better than those obtained when using single-layer graphene (n = 1) in a similar laser (285 ns / 1.6 μJ pulses [15]). However, as we discussed above, GSA shows rather high non-saturable losses (α'_{NS}/α') which are known to increase strongly with the increase of n due to scattering on the interlayer interfaces [9,10]. Such losses limit significantly the laser efficiency and reduce the conversion efficiency with respect to the CW mode of operation. Having in mind the modulation depth and non-saturable losses of the GSA, we consider n = 2...4 as optimum number of layers for GSA PQS of Tm-lasers. The value of α'_{NS} can be further reduced by improving the technology of synthesis of the multi-layer graphene samples.

Now let us discuss the influence of the laser material. For Q-switching, an important parameter of the gain medium is its energy storage capability expressed in terms of the lifetime of the upper laser level (e.g., $^3F_4$ level of Tm^{3+}). For GSA PQS of Tm lasers, an increase of the lifetime will lead to shortening of the laser pulses and a slight increase of their energy; however, this effect

is relatively weak. For instance, a 2-fold variation of the lifetime will lead to ~10% change of the above mentioned parameters. Consequently, we can conclude that Tm-doped materials with longer lifetimes (e.g., fluorides) will provide better pulse characteristics.

The cavity design is also important for optimizing the performance of the GSA passively Q-switched Tm lasers. As I_{sat} is relatively low for graphene at ~2 µm, the requirements to the laser cavity for saturation of the absorption are not as stringent as in the case of Yb lasers at ~1 µm. As a consequence, Tm lasers can be Q-switched with graphene using different geometries of the laser cavity. However, due to the very low modulation depth of graphene (~0.1...0.3%), when applied in a long laser cavity, it may produce µs-long pulses [4,13,14]. Thus, the use of a compact cavity design (e.g., microchip) is rather beneficial for reaching pulse durations of the order of ~100 ns or even shorter. The microchip concept offers the possibility of direct deposition of graphene on one of the faces of the laser crystal. The drawback of such a compact cavity is the heating of graphene by residual pump absorption, which can be avoided by coating this surface highly reflective for the pump.

Our modelling indicated that an important parameter of the cavity is the size of the laser mode in the crystal, w_L. The pulse energy for GSA passively Q-switched lasers is scaling with the laser mode size as $\sim w_L^2$. In a compact cavity, w_L is primarily determined by the thermal lens and cannot be easily varied. Thus, the microchip arrangement is more favorable for reduction of the pulse duration rather than for energy scaling. Contrary, long cavities may provide scaling of the pulse energy (up to few tens of µJ, as expected from the modelling). From our model we also determined that a proper selection of the OC is important to achieve a stable PQS laser performance. Large T_{OC} will not provide a sufficient level of intracavity intensity on the GSA for its saturation. Thus, in contrast to Tm lasers with "slow" SAs where the use of larger T_{OC} enables an increase of the pulse energy and reduces the probability of laser damage of the intracavity optical elements, in the case of graphene, $T_{OC} \approx 5\%$ is close to optimum as for larger T_{OC} the SA will not be saturated.

The developed model is in principle suitable to describe Tm lasers PQS with different, recently emerging "fast" SAs, e.g. single-walled carbon nanotubes (SWCNTs) operating around the E_{11} fundamental transition [38], graphene oxide, transition metal dichalcogenides (TMDs, e.g. MoS_2, WS_2, $MoSe_2$) [39], black phosphorus or topological insulators (Bi_2Te_3, Sb_2Te_3). However, for those materials exhibiting a more complicated band structure (as compared with graphene), e.g. SWCNTs or MoS_2, one may additionally involve the rate-equation model for the SA.

4. Conclusion

We report on a model describing diode-pumped Tm bulk lasers passively Q-switched with graphene-based SAs. This model predicts correctly the dependence of the pulse characteristics on the pump level, in particular, the shortening of the Q-switched pulses and the increase of their energy, which is specific for "fast" SAs. The potential of graphene for the generation of few-ns pulses at ~2 µm is discussed. It is shown that the low saturable absorption of graphene ($\alpha'_S/\alpha' \sim 0.04$) and, hence, the low modulation depth of the SA (in the range ~0.1...0.3%, depending on the number of graphene layers) is the main limiting factor for the performance of such passively Q-switched

lasers. The developed model may also be used for the description of bulk Tm laser PQS with various “fast” SAs.

In order to validate our model a compact microchip-like Tm:KLuW laser passively Q-switched with a transmission-type multi-layer GSA was experimentally studied. This laser was scaled up to ~1 W average output power at 1926 nm. The slope efficiency reached 39% and the conversion efficiency with respect to the CW mode of operation was as high as η_{conv} = 70%. Stable pulses, as short as 190 ns with an energy of ~4 μJ were achieved at a PRF of 260 kHz. Graphene is a promising SA for <100 ns pulse generation at PRF in the MHz range if further power scaling of Tm lasers is achieved and if the intracavity losses due to the non-saturable absorption of graphene are optimized.

Acknowledgements

This work was supported by the Spanish Government under projects MAT2013-47395-C4-4-R and TEC2014-55948-R, and by the Generalitat de Catalunya under project 2014SGR1358. F.D. acknowledges additional support through the ICREA academia award 2010ICREA-02 for excellence in research. This work is part of a project that has received funding from the European Union’s Horizon 2020 research and innovation programme under the Marie Skłodowska-Curie grant agreement No 657630. P.A. Loiko acknowledges financial support from the Government of the Russian Federation (Grant 074-U01) through ITMO Post-Doctoral Fellowship scheme.

References

1. R. C. Stoneman, L. Esterowitz, Opt. Lett. 15 (1990) 486–488.
2. H. Yu, V. Petrov, U. Griebner, D. Parisi, S. Veronesi, M. Tonelli, Opt. Lett. 37 (2012) 2544-2546.
3. R. Faoro, M. Kadankov, D. Parisi, S. Veronesi, M. Tonelli, V. Petrov, U. Griebner, M. Segura, X. Mateos, Opt. Lett. 37 (2012) 1517-1519.
4. G. Q. Xie, J. Ma, P. Lv, W. L. Gao, P. Yuan, L. J. Qian, H. H. Yu, H. J. Zhang, J. Y. Wang, D. Y. Tang, Opt. Mater. Express 2 (2012) 878–883.
5. C. Liu, C. Ye, Z. Luo, H. Cheng, D. Wu, Y. Zheng, Z. Liu, B. Qu, Opt. Express 21 (2013) 204-209.
6. J. Liu, Y. Wang, Z. Qu, X. Fan, Opt. Laser Technol. 44 (2012) 960-962.
7. A. K. Geim, K. S. Novoselov, Nat. Mater. 6 (2007) 183–191.
8. R. R. Nair, P. Blake, A. N. Grigorenko, K. S. Novoselov, T. J. Booth, T. Stauber, N. M. R. Peres, A. K. Geim, Science 320 (2008) 1308.
9. F. Zhang, S. Han, Y. Liu, Z. Wang, X. Xu, Appl. Phys. Lett. 106 (2015) 091102-1-5.
10. Q. Bao, H. Zhang, Y. Wang, Z. Ni, Y. Yan, Z. X. Shen, K. P. Loh, D. Y. Tang, Adv. Funct. Mater. 19 (2009) 3077–3083.
11. Q. Bao, H. Zhang, Z. Ni, Y. Wang, L. Polavarapu, Z. Shen, Q. H. Xu, D. Y. Tang, K. P. Loh, Nano Res. 4 (2011) 297–307.
12. G. Xing, H. Guo, X. Zhang, T. C. Sum, C. H. A. Huan, Opt. Express 18 (2010) 4564–4573.
13. Q. Wang, H. Teng, Y. Zou, Z. Zhang, D. Li, R. Wang, C. Gao, J. Lin, L. Guo, Z. Wei, Opt. Lett. 37 (2012) 395–397.
14. T. L. Feng, S. Z. Zhao, K. J. Yang, G. Q. Li, D. C. Li, J. Zhao, W. C. Qiao, J. Hou, Y. Yang, J. L. He, L. H. Zheng, Q. G. Wang, X. D. Xu, L. B. Su, J. Xu, Opt. Express 21 (2013) 24665–24673.
15. J. M. Serres, P. Loiko, X. Mateos, K. Yumashev, U. Griebner, V. Petrov, M. Aguiló, F. Díaz, Opt. Express 23 (2015) 14108-14113.
16. V. Petrov, M. C. Pujol, X. Mateos, O. Silvestre, S. Rivier, M. Aguilo, R. M. Sole, J. H. Liu, U. Griebner, F. Díaz, Laser Photon. Rev. 1 (2007) 179–212.
17. A. E. Troshin, V. E. Kisel, A. S. Yasukevich, N. V. Kuleshov, A. A. Pavlyuk, E. B. Dunina, A. A. Kornienko, Appl. Phys. B 86 (2007) 287–292.
18. O. Silvestre, M. C. Pujol, M. Rico, F. Güell, M. Aguiló, F. Díaz, Appl. Phys. B 87 (2007) 707–716.
19. S. Vatnik, I. Vedin, M. C. Pujol, X. Mateos, J. J. Carvajal, M. Aguiló, F. Díaz, U. Griebner, V. Petrov, Laser Phys. Lett. 7 (2010) 435-439.
20. X. Mateos, V. Petrov, J. Liu, M. C. Pujol, U. Griebner, M. Aguiló, F. Díaz, M. Galan, G. Viera, IEEE J. Quantum Electron. 42 (2006) 1008–1015.
21. S. M. Vatnik, I. A. Vedin, A. A. Pavlyuk, Laser Phys. Lett. 9 (2012) 765–769.
22. J.M. Serres, X. Mateos, P. Loiko, K. Yumashev, N. Kuleshov, V. Petrov, U. Griebner, M. Aguiló, F. Díaz, Opt. Lett. 39 (2014) 4247-4250.

23. M. Segura, M. Kadankov, X. Mateos, M. C. Pujol, J. J. Carvajal, M. Aguiló, F. Díaz, U. Griebner, V. Petrov, Opt. Express 20 (2012) 3394–3400.
24. M. S. Gaponenko, A. A. Onushchenko, V. E. Kisel, A. M. Malyarevich, K. V. Yumashev, N. V. Kuleshov, Laser Phys. Lett. 9 (2012) 291-294.
25. P. Loiko, J.M. Serres, X. Mateos, K. Yumashev, A. Yasukevich, V. Petrov, U. Griebner, M. Aguiló, F. Díaz, Opt. Lett. 40 (2015) 5220-5223.
26. J. J. Zayhowski, C. Dill, Opt. Lett. 19 (1994) 1427-1429.
27. J.M. Serres, P. Loiko, X. Mateos, V. Jambunathan, K. Yumashev, U. Griebner, V. Petrov, M. Aguiló, F. Díaz, Laser Phys. Lett. 13 (2016) 025801-1-5.
28. P. Loiko, M. Pollnau, J. Phys. Chem. C 120 (2016) 26480-26489.
29. S. So, J.I. Mackenzie, D.P. Shepherd, W.A. Clarkson, J.G. Betterton, E.K. Gorton, Appl. Phys. B 84 (2006) 389-393.
30. K. van Dalfsen, S. Aravazhi, C. Grivas, S. M. García-Blanco, M. Pollnau, Opt. Lett. 39 (2014) 4380-4383.
31. H. Haus, IEEE J. Quantum Electron. QE-12 (1976) 169-176.
32. J. M. Serres, V. Jambunathan, X. Mateos, P. Loiko, A. Lucianetti, T. Mocek, K. Yumashev, V. Petrov, U. Griebner, M. Aguiló, F. Díaz, IEEE Photonics J. 7 (2015) 1503307-1–7.
33. P. A. Loiko, J. M. Serres, X. Mateos, K. V. Yumashev, N. V. Kuleshov, V. Petrov, U. Griebner, M. Aguiló, F. Díaz, Laser Phys. Lett. 11 (2014) 075001-1-7.
34. A. A. Balandin, S. Ghosh, W. Bao, I. Calizo, D. Teweldebrhan, F. Miao, C. N. Lau, Nano Lett. 8 (2008) 902–907.
35. D. Yoon, Y. W. Son, H. Cheong, Nano Lett. 11 (2011) 3227–3231.
36. P. A. Loiko, J. M. Serres, X. Mateos, J. Liu, H. Zhang, A. S. Yasukevich, K. V. Yumashev, V. Petrov, U. Griebner, M. Aguiló, F. Díaz, Appl. Phys. B 122 (2016) 105-1–8.
37. R. Lan, P. Loiko, X. Mateos, Y. Wang, J. Li, Y. Pan, S. Y. Choi, M. H. Kim, F. Rotermund, A. Yasukevich, K. Yumashev, U. Griebner, V. Petrov, Appl. Opt. 55 (2016) 4877–4887.
38. P. Loiko, X. Mateos, S. Y. Choi, F. Rottermund, J. M. Serres, M. Aguiló, F. Díaz, K. Yumashev, U. Griebner, V. Petrov, J. Opt. Soc. Am. B 33 (2016) D19-D27.
39. J. M. Serres, P. Loiko, X. Mateos, H. Yu, H. Zhang, Y. Chen, V. Petrov, U. Griebner, K. Yumashev, M. Aguiló, and F. Díaz, Opt. Mater. Express 6 (2016) 3262-3273.

Figure captions

Figure 1 Scheme of energy levels and relevant processes for Tm^{3+} ion: ESA - excited-state absorption, CR - cross-relaxation, UCL - up-conversion luminescence.

Figure 2 Scheme of the saturable absorption process in graphene.

Figure 3 Set-up of the passively Q-switched Tm microchip laser with graphene as saturable absorber: LD - laser diode, PM - pump mirror, OC - output coupler.

Figure 4 (a) Transmission spectra of the single- and multi-layer graphene (Fresnel losses at SiO_2 substrate surfaces are subtracted), *inset* - image of the multi-layer graphene saturable absorber; (b) Raman spectrum of the multi-layer graphene.

Figure 5 Input-output dependence and typical laser emission spectrum (inset) for the multi-layer GSA passively Q-switched Tm:KLuW microchip laser.

Figure 6 Passively Q-switched Tm:KLuW microchip laser by a multi-layer GSA: pulse duration (FWHM) (a), pulse repetition frequency (PRF) (b), pulse energy (c) and peak power (d): *symbols* - experimental data, *curves* - modelling.

Figure 7 Intracavity peak laser intensity on GSA, I_{in}, and its intensity-dependent absorption, $\alpha'(I_{in})$, for GSA PQS Tm:KLuW microchip laser: *symbols* - values derived from the experimental data, *curves* - modelling.

Figure 8 Graphene saturable absorber passively Q-switched Tm: KLuW microchip laser: Oscilloscope traces of the single pulses at threshold and at the maximum absorbed power (a) and the pulse train at P_{abs} = 4.9 W (b).

Figure 9 Modeling of the laser output from a GSA PQS Tm:KLuW microchip laser: (a,b) single Q-switched pulse (a) and modeled pulse train (b) for P_{abs} = 4.9 W, $I'_{norm} = 25\times10^{-4}$; (c-f) modeled output including the onset of lasing for various normalized rates of noise intensity I'_{norm} = 35×10^{-4} (c), 32×10^{-4} (d), 28×10^{-4} (e) and 25×10^{-4} (f).

Figure 1

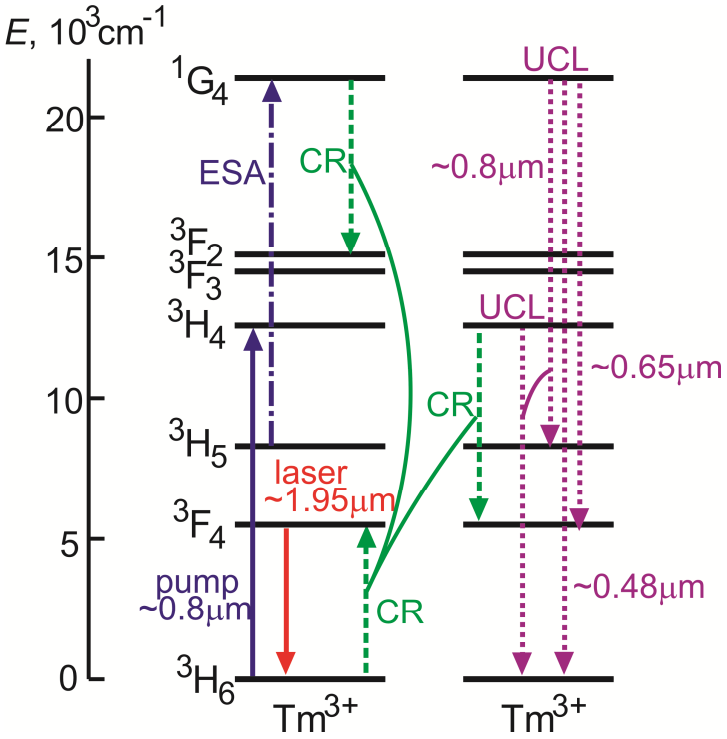

Figure 2

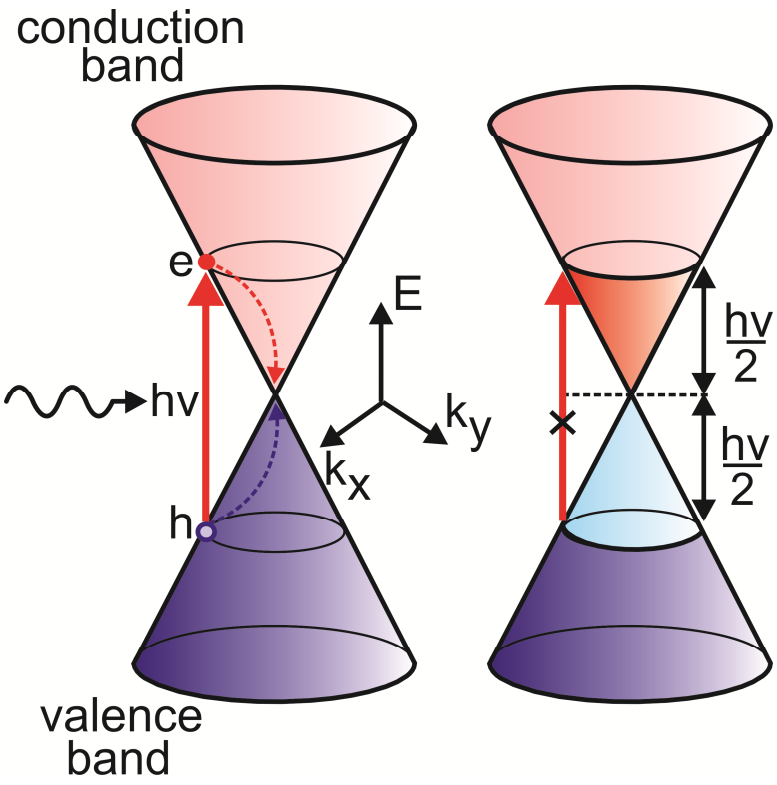

Figure 3

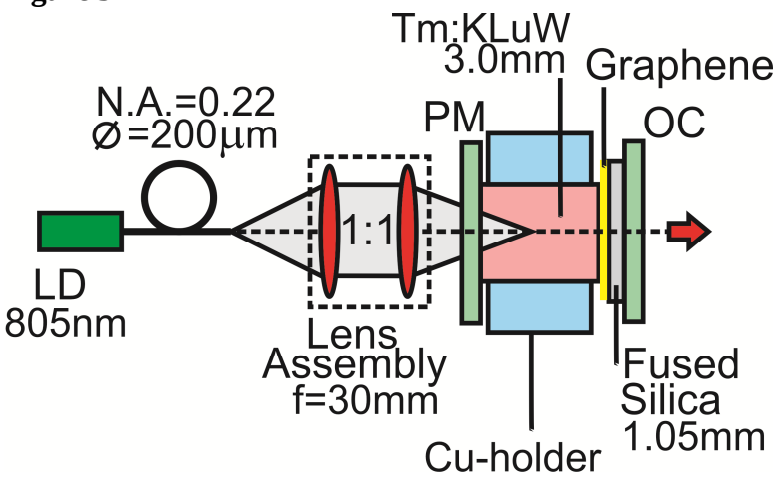

Figure 4

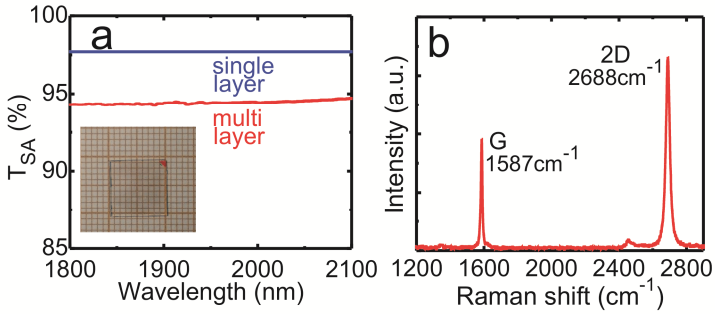

Figure 5

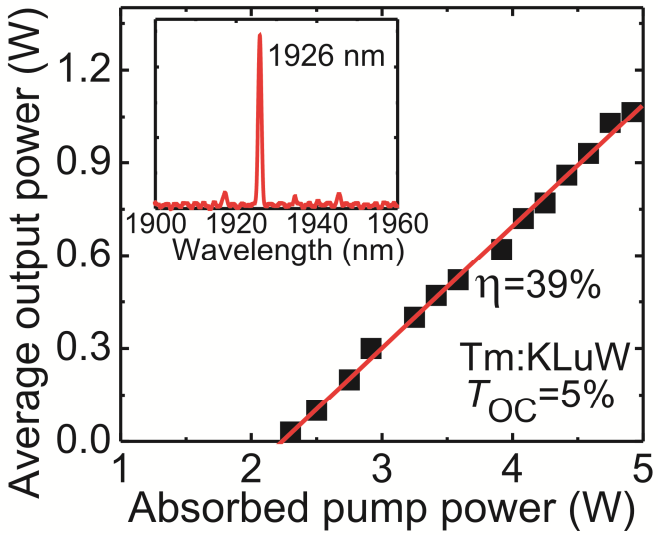

Figure 6

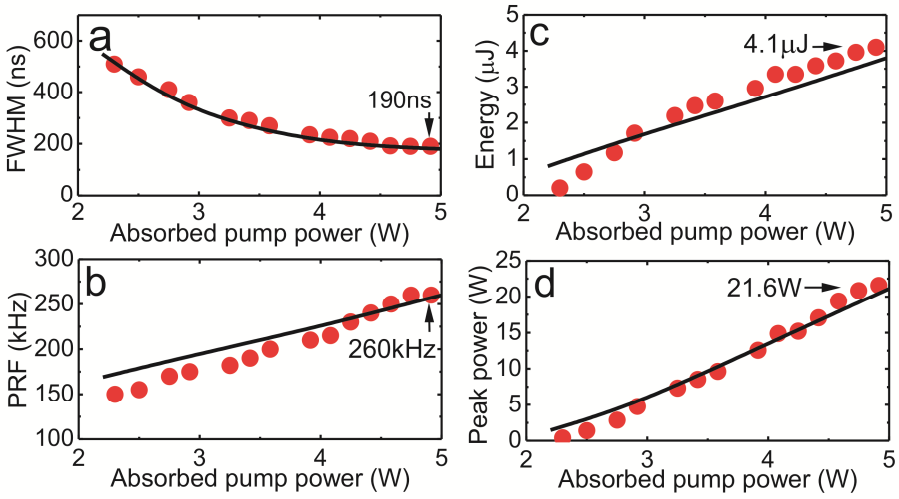

Figure 7

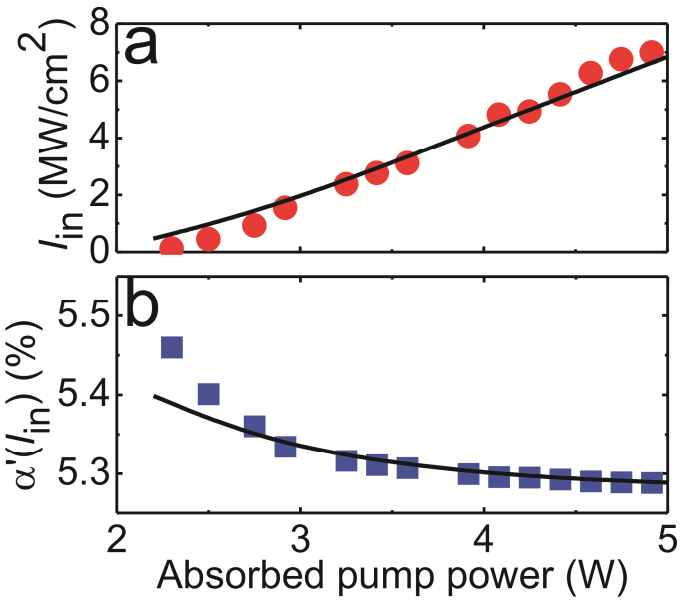

Figure 8

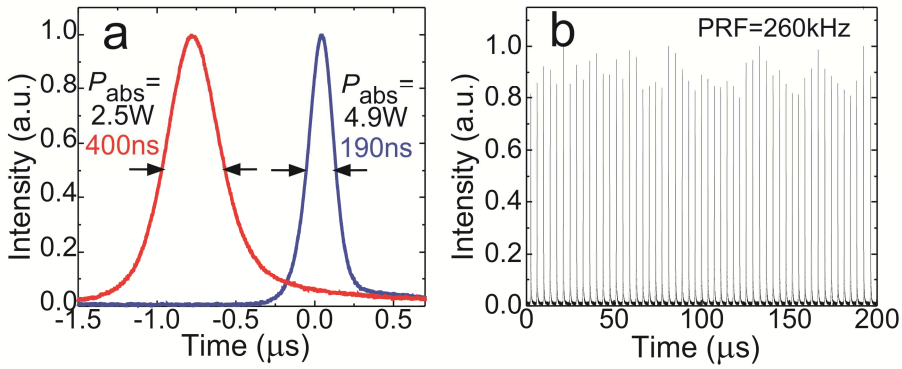

Figure 9